

Bulk single crystal growth of the theoretically predicted magnetic Weyl semimetals $RAlGe$ ($R = Pr, Ce$)

Pascal Puphal,^{1,*} Charles Mielke,¹ Neeraj Kumar,² Y. Soh,² Tian Shang,^{1,3}
Marisa Medarde,¹ Jonathan S. White,^{4,†} and Ekaterina Pomjakushina^{1,‡}

¹Laboratory for Multiscale Materials Experiments,
Paul Scherrer Institute, 5232 Villigen, Switzerland

²Paul Scherrer Institute, 5232 Villigen, Switzerland

³Ecole Polytechnique Fédérale de Lausanne (EPFL), Lausanne CH-1015, Switzerland.

⁴Laboratory for Neutron Scattering and Imaging,
Paul Scherrer Institute, 5232 Villigen, Switzerland

We explore two methods for single crystal growth of the theoretically proposed magnetic Weyl semimetals $RAlGe$ ($R = Pr, Ce$), which prove that a floating zone technique, being both crucible- and flux-free, is crucial to obtain perfectly stoichiometric $RAlGe$ crystals. In contrast, the crystals grown by a flux growth technique tend to be Al-rich. We further present both structural and elemental analysis, along with bulk magnetization and electrical resistivity data on the crystals prepared by the floating zone technique. Both systems with the intended 1:1:1 stoichiometry crystallize in the anticipated polar $I4_1md$ (No. 109) space group, although neither displays the theoretically expected ferromagnetic ground state. Instead $PrAlGe$ displays a spin-glass-like transition below 16 K with an easy-c-axis and $CeAlGe$ has an easy-ab-plane antiferromagnetic order below 5 K. The grown crystals provide an ideal platform for microscopic studies of the magnetic field-tunable correlation physics involving magnetism and topological Weyl nodes.

I. INTRODUCTION

In 1929, Hermann Weyl suggested a solution to the Dirac equation for fermions in terms of massless particles, the so-called Weyl fermions[1]. Only recently, however, has experimental evidence for their existence as quasiparticles in $(Ta, Nb)As$ [2–4] been presented, leading to these compounds being known as Weyl semimetals. The hallmark feature of these materials are topologically non-trivial band touching points – the Weyl nodes – in their electronic spectra [5, 6], which can endow the host system with technologically promising properties in fields ranging from catalysis [7, 8] to optoelectronics [9, 10].

The most versatile possibilities for Weyl node formation is in systems displaying simultaneously broken spatial inversion (SI) and time reversal (TR) symmetries. With TR symmetry broken naturally by the onset of magnetic order, magnetic semimetals are ideal candidates for studying the magnetic field-tunable correlation between magnetism and Weyl physics [10]. Indeed, the influence of Weyl nodes on the transport properties has been evidenced in some magnetic systems [11–13], motivating the study of the associated phenomena that is of both fundamental and technological importance [14].

From recent first principles theoretical calculations, it has been predicted that the members of the $RAlGe$ ($R = Pr, Ce$) system are new magnetic Weyl semimetals [15] that offer remarkable tunability, since the number and location of Weyl nodes may be controlled by choice of the rare earth element [15] and the types of the broken symmetry, i.e. SI and/or TR, via the Al/Ge content. In addition, in the presence of the combined broken symmetries, the system offers a rich phase diagram that may be

explored via self-doping or chemical substitution. Therefore, to enable a broad range of experimental studies on this class of material, there is a clear interest for establishing the details for the growth of sizable ($\sim mm^3$) single crystals and their basic physical characterization.

First discovered in 1992, $RAlGe$ was initially described to crystallize in the so called $\alpha-ThSi_2$ structure-type with a centrosymmetric space group $I4_1/amd$ (No. 141) [16]. Later on however, it has been realized instead that $RAlGe$ crystallizes in the $LaPtSi$ -type structure [17, 18], with a body-centered tetragonal Bravais lattice and a polar, i.e. SI breaking, space group $I4_1md$ (No. 109). A subsequent study of the silicon variants RAl_xSi_{2-x} revealed a tunability of the structure-type according to the Si content [19]. It was established that single crystals including all Lanthanides could be prepared in quartz ampoules using the high-temperature flux technique with molten Al as a solvent, and the flux removed by centrifugation [19]. Due to both the evaporation and reaction of Al with quartz, a fast-cooling rate was implemented in order to avoid a breaking of the ampoules.

To date, little is known about the physical properties of $RAlGe$. For $PrAlGe$, there is only a detailed study of the crystal structure [18], with no physical property characterization. For $CeAlGe$ contradictory results are published for the magnetic properties; early bulk susceptibility data show the magnetic Ce ions to order below ~ 6 K, but the system has been reported to order as a ferromagnet (FM) [20] and an antiferromagnet (AFM) [17]. Most recently, a study on flux grown $CeAlGe$ single crystals was reported [21], with bulk magnetization measurements evidencing ferromagnetic coupling in one direction, and antiferromagnetic coupling in another, ap-

parently resolving contradictions so far. In more detail, the identified easy-axis of [100] suggested antiferromagnetic order in the ab-plane.

Importantly however, the crystals studied in Ref. [21] were prepared following the same route as reported in Ref. [19], using SiO₂ ampoules. As discussed in Ref. [19, 21], this choice of ampoule often leads to Si inclusions and a stable co-existing CeAlSi phase, while at the same time, samples that are even slightly Al-rich can lead to different crystal structures that maintains SI symmetry [17, 21], thus greatly limiting the propensity for the formation of topological Weyl nodes. Therefore, a stoichiometric analysis is necessary to ensure the intended 1:1:1 stoichiometry of RAlGe is achieved, and we will show that this is less likely to be achieved in flux-grown samples compared with crystals grown by the floating zone method.

Here we present the successful single crystal growth of both PrAlGe and CeAlGe, first by Al self-flux growth without the use of quartz ampoules, and secondly using crucible-free bulk crystal growth in a floating zone in a mirror furnace. Only by the latter approach truly stoichiometric single crystals were obtained reliably. In addition, we performed differential thermal analysis (DTA) to optimize the flux profile and find the melting points. Finally we present both a magnetic characterization and transport data obtained from the single crystals, with the results confirming that the crystals have physical properties consistent with those expected for magnetic semimetals.

II. EXPERIMENTAL DETAILS

For the flux growth a home built tubular furnace was used that was connected to vacuum and argon lines.

Thermogravimetric analysis was performed using a NETZSCH STA 449C analyser.

The polycrystalline rods for the floating zone growth were cast in a SCIDRE KTS - levitation melting facility. By induction melting, the three starting elements Ce/Pr, Al and Ge of a minimum purity of 99.99% are levitated in a strongly changing magnetic field, followed by a sudden switching-off so that the melt falls into a cooled copper shaper. The floating zone growth was performed in a SCIDRE HKZ - high pressure, high-temperature, optical floating zone furnace.

The powder x-ray diffraction was performed using a Bruker D8 Advance with a Cu cathode.

Energy dispersive X-ray spectra (EDS) were recorded with an AMETEK EDAX Quanta 400 detector in a Zeiss DSM 940A scanning electron microscope (SEM).

Magnetic susceptibility measurements were carried out in a range of 1.8 - 400 K and 0 - 7 T using a Quantum Design Magnetic Property Measurements System (MPMS). Resistivity measurements were carried out for the range

of 1.8 - 300 K and 0 - 4 T, as well as and AC measurements from 10 - 20 K on a Quantum Design Physical Property Measurement System (PPMS).

III. CRYSTAL GROWTH

A. DTA analysis

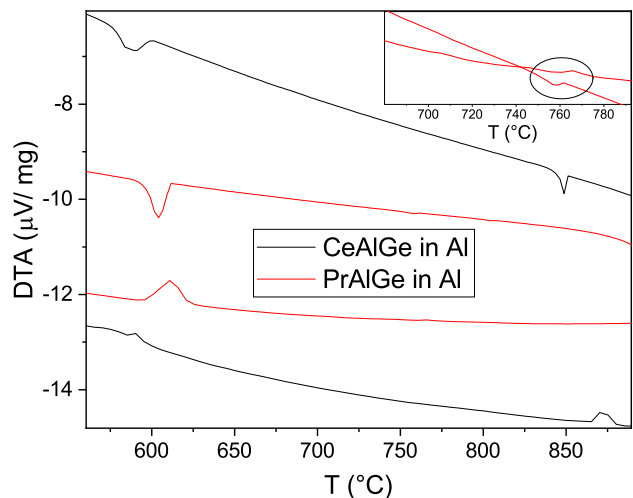


Figure 1. Extract of DTA curves of polycrystalline CeAlGe (black) and PrAlGe (red) samples measured in the presence of 20 moles of Al flux at a quick heating and cooling rate of 10 K/min in the range of 300°C to 950°C. The first signal around 600°C corresponds to the melting and crystallization of the Al flux. The inset shows a magnification of the PrAlGe DTA curve.

For both CeAlGe and PrAlGe we performed differential thermal analysis (DTA) runs solely on the stoichiometric 1:1:1 mixture of reacted materials obtained by arc melting (see sub-section D) as well as in Al-flux, both in a reducing atmosphere with a He(95%)-H₂(5%) gas flow of 60 cc/min. For a measurement on the polycrystalline RAlGe samples without flux (data not shown) we could see no pronounced DTA peaks denoting a melting up to 1500°C, proving them to have a higher melting point. However, the dissolution and crystallization points of CeAlGe and PrAlGe in aluminum flux were found to be at 860°C (see black curves of Fig. 1) and 760°C (see red curves of Fig. 1), respectively.

B. Flux growth

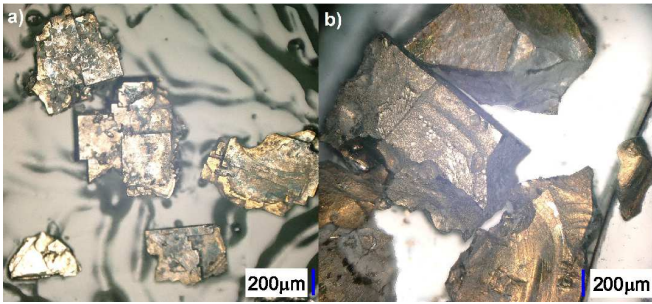


Figure 2. Pictures of the flux-grown crystals of a) CeAlGe and b) PrAlGe right after flux removal using NaOH-H₂O, and before subsequent annealing.

Aiming to obtain sizeable $\sim\text{mm}^3$ crystals, we chose to perform flux growth without quartz ampules, and used instead up-scaled alumina crucibles of a large volume (100 ml) and performed the growth under argon atmosphere. This choice also provides the opportunity to refine the previously published growth profile given in Ref. [19]. There, the authors used a thermal ramping rate of $200^\circ\text{C}/\text{h}$ to the reaction temperature of 1175°C , held for 2 h, followed by cooling to 700°C at a rate of $30^\circ\text{C}/\text{h}$, where the Al flux was effectively removed by centrifugation. In our approach, the flux was removed by dissolution in a NaOH-H₂O solution.

Similarly to Ref. [19], we used a R:Ge:Al ratio of 1:1:20 with 20 g of aluminum granules, 5.2 g Ce/ 5.3 g Pr pieces cut freshly from a rod in a He glove-box, and 2.69 g Ge pieces. These were all placed in a Al₂O₃ crucible that was placed inside the tubular furnace. The optimal growth profile was found with a quick heating of $300^\circ\text{C}/\text{h}$ going up to 950°C , held for 2 h and then slowly cooled at $2.5^\circ\text{C}/\text{h}$ to 685°C , followed by a quick cooling. We chose a maximum temperature of 950°C since this higher temperature compared to the dissolution point improved the homogenisation and mixing. Afterwards, the whole piece displayed increased oxidation on the surface due to both an oxide layer from the alumina granules, and traces of oxygen in the argon gas due to the porosity of the furnace-tube, but the crystals on the bottom were not affected. The crucible was then placed in a NaOH-H₂O solution at 150°C until only the plate-like crystals were left and could be filtrated. The general habit of the crystals obtained was quite different between the two systems; for CeAlGe (see Fig. 2 a) the crystals grow typically for tetragonal systems in terrace shapes and as quite thin *c*-axis platelets, while the PrAlGe crystals grow with sizable proportions along the *c*-axis, and as bulky pieces (see Fig. 2 b). For both crystal species, some aluminum flux on the surfaces remained that could not be removed by the base, as further discussed in section IV.

The crystals were then put into fused silica ampules and annealed at 1100°C for one week, leading to a darker appearance.

C. Floating zone growth



Figure 3. Photos of a) the cast CeAlGe rod, and the floating zone grown crystals of b) CeAlGe and c) PrAlGe.

The starting rods for the floating zone crystal growth were cast using a stoichiometric mixture of Ce or Pr, Al and Ge. Ce-pieces were freshly cut from a rod in a He glovebox and corresponding amounts of Al and Ge pieces were weighed. The materials were then transferred to the levitation melting facility (KTS) equipped with a quartz tube. The quartz chamber was flushed with Ar gas. 25 g of starting material was found to be sufficient for casting the rods using the KTS machine, and rods were obtained like those shown in Fig. 3 a. CeAlGe proves to have a higher melting point than PrAlGe; it starts to melt at a power around 50% of the 40 kW and 100 kHz generator with a proper fluidity achieved at a power of 70% enabling the casting. In contrast, PrAlGe is homogeneously molten at just 45% power. When CeAlGe melts, a slight evaporation is observed, which is mainly due to Al and is manifested as a tiny vapour pressure that develops at 1400°C , while Ce starts melting at 1900°C . The deduction that Al was evaporating was confirmed by reduced Al content on repeatedly cast rods measured by energy dispersive X-ray analysis (EDS).

The rods were then placed and centered in the high pressure, high-temperature optical floating zone furnace (HKZ). After pumping the sapphire chamber, a purification process of Ar was started in a flow of 0.11/min. The power was then slowly ramped up and we could pre-melt and connect the rods at 30% power of the 5kW Xenon lamp for CeAlGe and 20% for PrAlGe. A temperature check using a pyrometer lets us deduce a melting point slightly above $\sim 1500^\circ\text{C}$ for PrAlGe and $\sim 1600^\circ\text{C}$ for CeAlGe. For CeAlGe, we chose a higher pressure of 30 bar argon compared with 5 bar for PrAlGe, to suppress the described evaporation. The presence of RAlO₃ traces causes a particular behavior of the melt whereby

the oxide moves to the surface and forms a solid layer around the liquid part, causing some shaking. However, it also helped to keep a stable liquid, and enable a simple necking.

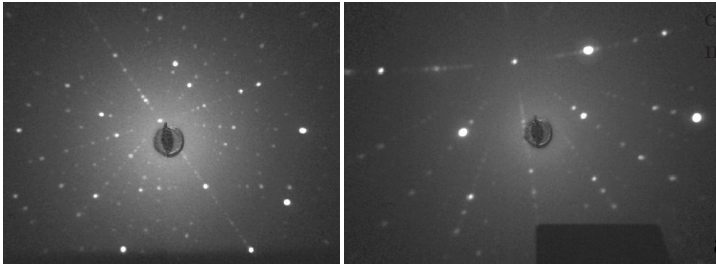


Figure 4. Backscattered x-ray Laue images from the PrAlGe crystal taken along and perpendicular to the growth direction. The images revealed a slight tilt of the a/b - (first image) and c - (second) axis with respect to the principal growth axes.

By exploring different growth rates (1 - 20 mm/h), we have found that in the case of PrAlGe a quick growth rate of 12 mm/h leads to two dominant grains developing after a few millimeter of growth, which grow equally quickly over the whole growth volume. For the case of CeAlGe, such fast growth rates do not result in big crystalline grains. We achieved the best result with a growth rate of 1 mm/h, where several (two or more) large mm sized grains develop over the very last cm of the grown crystal from a total crystal length up to 10 cm.

Due to the migration of $RAlO_3$ to the surface during the growth, the resulting crystal appears less shiny than the starting polycrystalline rod. This oxide layer can be removed easily by polishing. For both materials, an x-ray Laue analysis revealed a tendency for growth along an a -direction, with the c - and the second a -directions aligned perpendicular to the rod surface. Being reasonably brittle, little force is required to break the crystal, showing highly symmetric, cleaved surfaces to separate the grains. We further note that CeAlGe is less stable in air than PrAlGe, with a certain smell noticed when being polished and sparks when being crushed. However, it oxidizes slowly and builds a passivation layer similarly as pure Ce. Crystals cut with a water-cooled diamond saw decayed partly into CeO_2 and broke into several pieces. PrAlGe, on the other hand, showed no such features and seems to be more stable in air.

D. Polycrystalline $CeAl_xGe_{2-x}$

To provide a better insight into the effect of stoichiometry, we produced polycrystalline samples of $CeAl_{1.1}Ge_{0.9}$ and $CeAl_{0.9}Ge_{1.1}$ by arc melting the respective stoichiometric mixture of Ce, Al and Ge pieces prepared in the same way as the rods. The samples were then characterized by X-ray diffraction. Attempts to synthesize

$CeAl_{1.5}Ge_{0.5}$ gave rise to $CeAl_4$ impurities, while the attempt to synthesize $CeAl_{0.5}Ge_{1.5}$ yielded $Ce_2Al_3Ge_4$. We found that phase pure samples could be obtained by reducing the substitution level down to 10% ($CeAl_{1.1}Ge_{0.9}$ and $CeAl_{0.9}Ge_{1.1}$). As a last step, the stoichiometry was checked by EDS analysis to ensure a homogeneous elemental distribution.

IV. CRYSTAL STRUCTURE

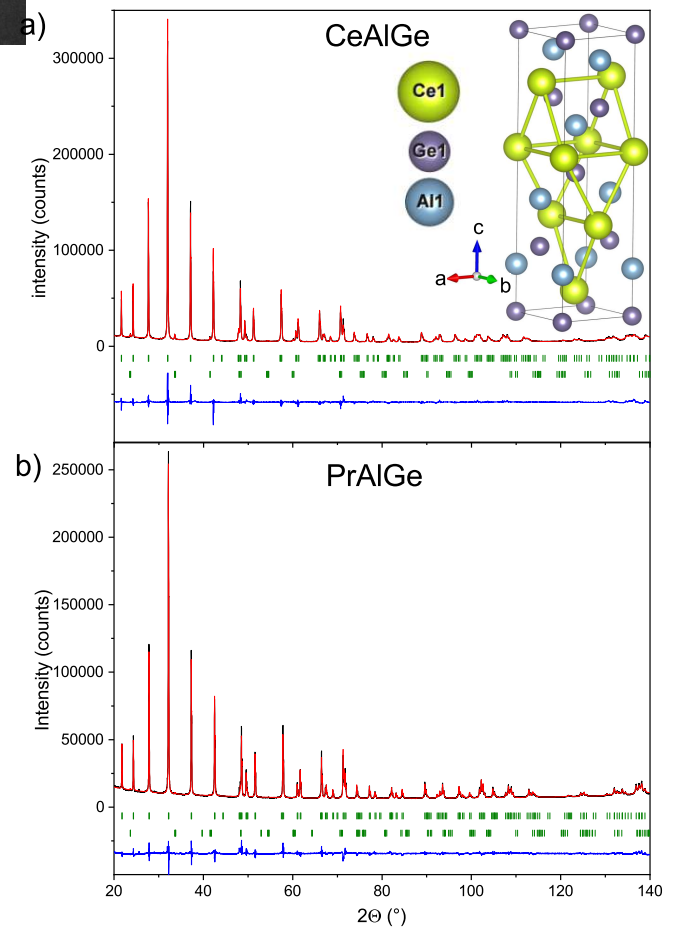


Figure 5. Rietveld refinement of the crystal structure parameters of both compounds from PXRD data. The observed intensity (black), calculated profile (red), and difference curve (blue) are shown for crushed crystals obtained by the floating zone technique of a) CeAlGe and b) PrAlGe. The rows of ticks at the bottom correspond to the calculated diffraction peak positions of the phases (from top to bottom): a) CeAlGe 97.7(5) wt% and $CeAlO_3$ 2.3(1) wt% b) PrAlGe 99.3(4) wt%, $PrAlO_3$ 0.7(0) wt% . Inset: an image of the refined $I4_1md$ (No. 109) structure is shown.

As mentioned in the introduction, CeAlGe was first reported to crystallize in the α - $ThSi_2$ structure-type with space group $I4_1/amd$ (No. 141) [16], with later studies

Table I. Crystallographic data of CeAlGe and PrAlGe obtained by powder X-ray diffraction (PXRD) performed at 295 K on crushed single crystals obtained both by the floating zone and the flux-technique. Space group $I4_1md$ (No. 109) with all atoms in the (4a) position (0 0 z).

compound	CeAlGe (floating zone)		CeAlGe (flux)		PrAlGe (floating zone)		PrAlGe (flux)		
EDS	Ce _{1.02(7)}	Al _{1.01(16)}	Ge _{0.97(9)}	Ce _{1.0(1)}	Al _{1.12(1)}	Ge _{0.88(1)}	Pr _{1.0(1)}	Al _{1.14(1)}	Ge _{0.86(1)}
a [\AA]	4.28155(1)		4.28978(4)		4.25009(1)		4.26330(4)		
c [\AA]	14.6919(6)		14.73222(16)		14.62316(5)		14.69512(18)		
R factor	4.59		7.16		2.99		7.59		
	z	U	z	U	z	U	z	U	
R	0.59235	0.00533(2)	0.58991	0.0047(6)	0.60832	0.0055(1)	0.60725	0.00433(8)	
Al	0.17736	0.01529(5)	0.17412	0.0248(14)	0.19040	0.0212(3)	0.19350	0.01014(18)	
Ge	0.01049	0.01529(5)	0.00686	0.0248(14)	0.02570	0.0212(3)	0.02435	0.01014(18)	

instead proposing the LaPtSi structure-type [17, 18] with a body-centered polar tetragonal space-group $I4_1md$ (No. 109) - see table I. The latter structure is shown in the inset of Fig. 5 a). The difference between this structure and the α -ThSi₂ type is that while the Al and Ge atoms occupy sites of different Wyckoff symmetry for the $I4_1md$ structure, they occupy a symmetry equivalent position in the $I4_1/amd$ case with 50% occupation of each element leading to an inversion center. Our refinement of PXRD data obtained from stoichiometric crushed single crystals obtained by the floating zone technique confirms the $I4_1md$ (No. 109) spacegroup, as it describes the data better than $I4_1/amd$. This is not only borne out by the refinement with the $I4_1md$ spacegroup yielding a lower R-factor, but we also find that if one tries to include site mixing in the $I4_1md$ case, there is no Al on the Ge site and vice versa. As expected, and as described in Section II C, a small amount of oxidized $RAlO_3$ is detected. The larger impurity phase fraction for CeAlGe compared to PrAlGe is due to the slow oxidation of the compound in air, which is enhanced in powder samples owing to the large surface. A refinement of the PXRD pattern on crushed crystals obtained from Al-flux show a larger unit cell strongly suggesting an enhanced Al content which has a larger crystal radius with 0.675 \AA compared to 0.67 \AA of Ge both in sixfold coordination.

V. ELEMENTAL ANALYSIS (EDS)

Using a scanning electron microscope (SEM), we performed an EDS analysis on several powder and single crystal samples prepared by all the above-described methods. This characterization is crucial, since both the structure-type and physical property transition temperatures can vary according to small compositional variations of RAl_xGe_{2-x} [17, 21].

As discussed in the introduction, flux growth has several issues, e.g. if SiO₂ ampoules are used, Si can be incorporated into the structure. We avoided this simply by performing the growth in an Al₂O₃ crucible and under an argon flow. Due to the application of Al self-flux, however, the tendency for substitution of Ge by extra Al

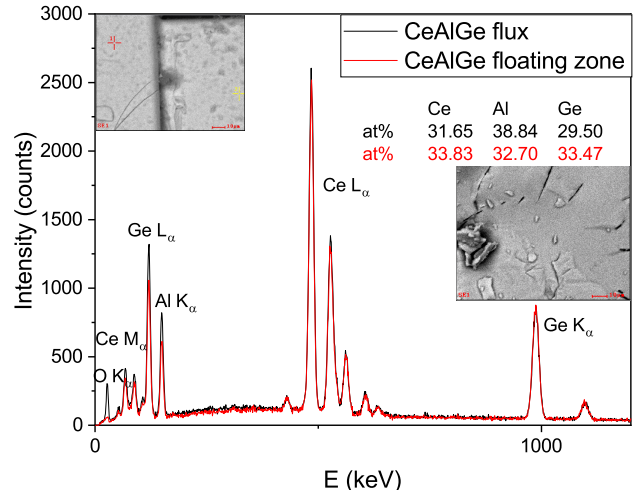


Figure 6. Typical EDS spectra from the surfaces of two CeAlGe single crystals measured in an SEM with the corresponding images as insets (topleft: flux grown, bottom right: floating zone grown crystal).

was observed in the crystals apparent from the EDS and PXRD refinement results shown in table I. For CeAlGe grown by Al-flux the resulting average stoichiometry on the surface was Ce_{1.0(2)}Al_{1.3(5)}Ge_{0.7(3)} and on a cleavage plane Ce_{1.0(1)}Al_{1.12(1)}Ge_{0.88(1)}. The given values are averages taken over at least 5 points on several samples, and the resulting statistical deviation is given in brackets. In addition, we observe some remaining Al₂O₃ on the surface of the crystals which can be seen as darker contrast in the SEM image shown as the left inset of Fig. 6. Similar results are obtained for PrAlGe samples with Pr_{1.0(1)}Al_{1.2(2)}Ge_{0.8(2)} measured on the surface and Pr_{1.0(1)}Al_{1.14(1)}Ge_{0.86(1)} on a polished crystal.

EDS measurements done on floating zone crystals shows them to be systematically much closer to the intended 1:1:1 stoichiometry, which can be expected for a crucible free growth in a congruently melting system, and where there is an absence of a minimum evaporation of volatile compounds. The average measured stoichiometries on cleaved surfaces as described

in chapter III. C. are $\text{Ce}_{1.02(7)}\text{Al}_{1.01(16)}\text{Ge}_{0.97(9)}$ and $\text{Pr}_{1.08(24)}\text{Al}_{0.97(7)}\text{Ge}_{0.95(17)}$. The polycrystalline samples of 10% Al over and underdoping show a measured stoichiometry of $\text{Ce}_{1.02(1)}\text{Al}_{1.14(1)}\text{Ge}_{0.84(1)}$ and $\text{Ce}_{1.06(5)}\text{Al}_{0.83(12)}\text{Ge}_{1.11(6)}$, respectively.

VI. BULK MAGNETIC AND TRANSPORT PROPERTIES

A. CeAlGe

While there is no publication on magnetic properties of PrAlGe, bulk magnetic data from CeAlGe is mentioned in Refs. [16, 17, 21]. Due to the crystal field, Ce^{3+} ions are expected to form a doublet ground state that carries an effective spin-1/2, and which are coupled via the Ruderman-Kittel-Kasuya-Yosida (RKKY) interaction. Previously, an AFM transition was reported at $T_N = 4$ K [16, 17] or ~ 5 K [21], with a relatively low entropy of 5.3 J/mol K [16] or $0.75 R \ln 2 \approx 4.32$ J/mol K [21] compared with the theoretical value of 5.76 J/mol K for a spin 1/2 system. This effect should not be associated with Kondo screening since the Sommerfeld coefficient (~ 20 mJ/mol K [16, 17]) and resistivity measurements indicate a normal magnetically ordered $4f$ compound. Therefore, we assign the missing entropy to lie within the low temperature tail $\rightarrow 0$ K. The reported Curie-Weiss temperatures on polycrystals are $\Theta_W = -13.5$ K [17] or $\Theta_W = -3.6$ K [21] and an effective moment of $\mu_{eff} \approx 2.57 \mu_B$ [17, 21] indicates a Ce^{3+} valence.

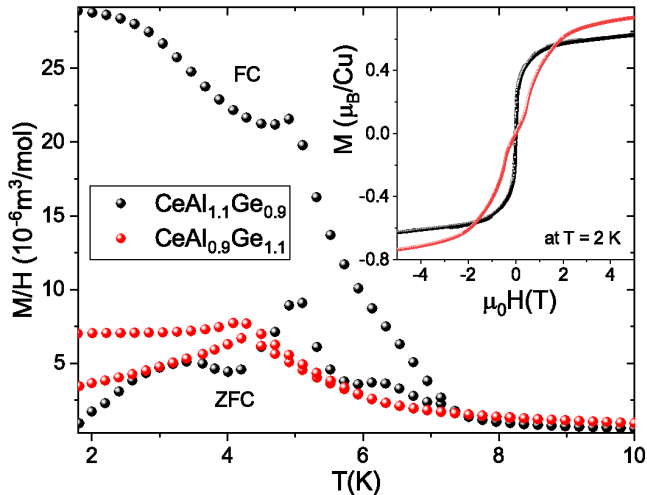


Figure 7. Low temperature magnetization measured in zero field cooled and field cooled manner on a powder sample of 22 mg ($x = 1.1$) and 20 mg ($x = 0.9$) of $\text{CeAl}_x\text{Ge}_{2-x}$ in a field of 5 mT. The inset shows the corresponding field dependence of the magnetization measured at 2 K.

When discussing bulk measurements, we show first that the exact values of characteristic physical proper-

ties are sensitive to the precise stoichiometry, as was discussed previously, for example, in the context of Fig. 4 in Ref. [17]. Therefore, the stoichiometric variations between the samples provides a natural explanation for differences in properties reported in the literature. To provide a better insight into the effect of stoichiometric differences, we present first magnetic measurements of polycrystalline samples of $\text{CeAl}_{1.1}\text{Ge}_{0.9}$ and $\text{CeAl}_{0.9}\text{Ge}_{1.1}$. The temperature-dependent magnetic susceptibility of the samples was measured in the MPMS and the resulting low temperature part is shown in Fig. 7. The data show the first magnetic ordering transition temperatures indeed display a pronounced dependence on the stoichiometry. For the Al-deficient sample, we observe a kink in the susceptibility denoting an antiferromagnetic transition near 4 K, similarly as reported in Ref. [16, 17]. On the other hand, the Al-rich sample shows a more irregular thermal behavior, showing a ferromagnetic-like transition near 7 K, followed by an antiferromagnetic-like one close to 5 K. As found in field dependent-magnetization a metamagnetic transition at 3.6 T occurs in the Al-deficient variant, which is absent in the Al-rich sample. This strong sensitivity of the magnetic properties to the stoichiometry clarifies the reason for a conflicting picture of the ground state provided by previous reports, and proves the necessity for well-characterized crystals when exploring physical phenomena in such samples.

With this in mind, we focus now on the characterization of relatively large single crystals obtained via the floating zone technique.

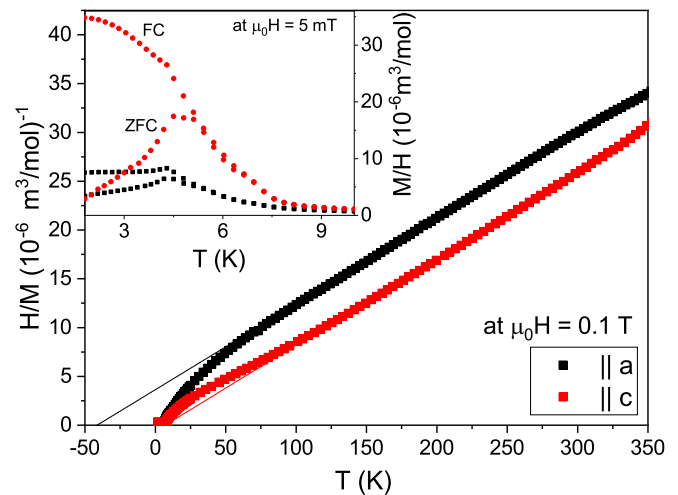


Figure 8. Magnetic data obtained on a floating zone grown CeAlGe single crystal with a mass of 125.4 mg. The magnetic susceptibility was measured in the range of 1.8 - 400 K with the field aligned parallel to a (black dots) and parallel to c (red dots). The main figure shows the inverse susceptibility obtained after field cooling at 0.1 T. Inset: The low temperature range of both zero field cooled and field cooled magnetic susceptibility curves measured in 5 mT.

In Fig. 8 the temperature-dependent inverse susceptibility H/M of CeAlGe measured in a field of 0.1 T is shown for H along both the a - and c -axes. Curie-Weiss fits of the high temperature part of the data reveal a ferromagnetic Weiss-temperature along the c -axis with $\Theta_W \approx 10$ K and an antiferromagnetic one along the a -axis with $\Theta_W \approx -42$ K. In both cases, the effective moment obtained by fitting the high temperature part of the data is $\mu_{eff} \approx 2.69 \mu_B$, this being slightly larger than the theoretical one of $\mu_{eff}^{Ce^{3+}} = 2.54 \mu_B$. In the inset of Fig. 8, the low temperature part of the susceptibility for both field directions in an applied field of 5 mT is shown after both field-cooling (FC) and zero-field-cooling (ZFC). In each case, a maximum is observed indicating an AFM order to onset at 4.5 K (field parallel to c) and 4.3 K (field parallel to a). The magnetic anisotropy is also visible in terms of a stronger difference between FC- and ZFC-curves for fields parallel to c .

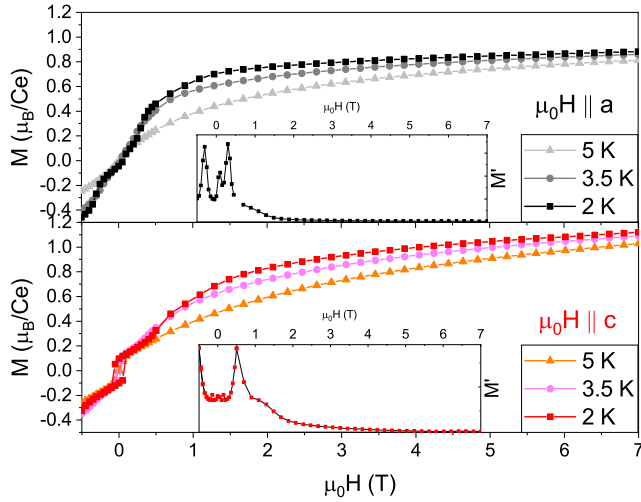


Figure 9. Field-dependence of the magnetization measured on a 125.4 mg floating zone grown CeAlGe single crystal at 2 K, 3.5 K, and 5 K for both field directions: parallel to a (black/gray symbols) and c (red/pink/orange symbols). Insets show the magnetic field derivative of the corresponding 2 K dataset.

In Fig. 9, the field dependent magnetization is shown for the field both parallel to a and c , and at three different temperatures of 2 K, 3.5 K, and 5 K around the AFM transition. For both field directions, a metamagnetic transition is apparent, as seen clearly in the field-derivatives shown as corresponding insets in Fig. 9. The obtained values for the metamagnetic transition fields are ~ 0.3 T for $H \parallel a$ and ~ 0.6 T for $H \parallel c$. A further transition for fields applied parallel to a is observed at a lower field of around 0.1 T, similarly as reported on the flux-grown samples [21]. At 7 T, the saturation magnetization M_s is not reached as we still observe a slight increase; at 2 K the value of the magnetization is larger along the c -direction with $1.12 \mu_B/Ce^{3+}$ compared to $0.88 \mu_B/Ce^{3+}$

for fields along the a -direction. A small hysteresis is visible with a coercivity of $h_c \sim 70$ mT and a remanence of $0.11 \mu_B$ for fields along c .

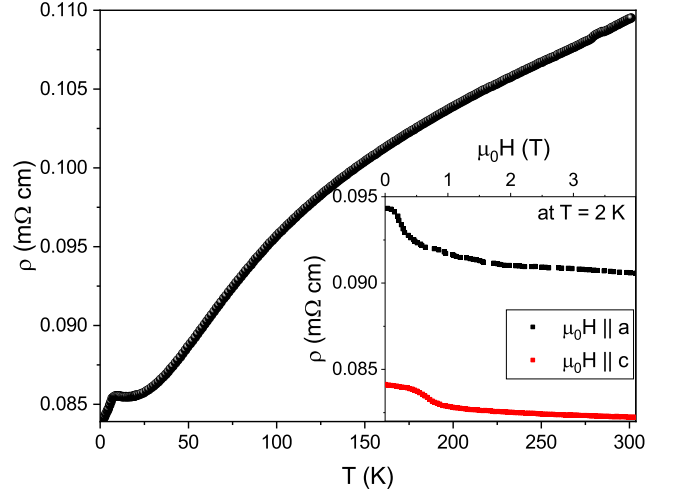


Figure 10. Temperature dependence of the resistivity with the current running along the a -direction on a needle like cut of 2.09 mg from a floating zone grown CeAlGe single crystal. The inset shows the field dependent resistivity with fields parallel to c and the current along a (red symbols), and fields parallel to a while the current runs along c (black symbols).

The temperature dependent resistivity data in zero field for a floating zone grown CeAlGe crystal piece is shown in Fig. 10. The estimated residual resistivity ratio (RRR) is 1.3 which is a relatively low value even for a semimetal [22], nonetheless it is comparable to that reported for flux grown crystals of 2.3 [17] and 2 [21]. The magnetic transition is visible as a slight maximum in the expected temperature region. In the bottom right inset of figure 10, the field dependent resistivity for fields applied both along the a - and the c -axes is shown to display a negative magnetoresistance. These data show anomalies at the metamagnetic transitions at around 0.3 T ($H \parallel a$) and 0.6 T ($H \parallel c$) in agreement with measurements obtained by $M(H)$.

B. PrAlGe

In Fig. 11, we show the temperature dependent inverse susceptibility H/M of a PrAlGe crystal measured either with a field of 0.1 T along the a - and c -axis. A Curie-Weiss fit of the data reveals a ferromagnetic Weiss-temperature along the c -axis with $\Theta_W \sim 36$ K and an antiferromagnetic one in the ab plane with $\Theta_W \sim -30$ K. The resulting effective moments are $\mu_{eff}^c \approx 4.1 \mu_B$ and $\mu_{eff}^a \approx 3.3 \mu_B$ with a resulting powder value of $\mu_{eff} = 2\mu_{eff}^a + \mu_{eff}^c = 3.57 \mu_B$ close to the theoretical one of $\mu_{eff}^{Pr^{3+}} = 3.58 \mu_B$. The inset of Fig. 11 shows the low temperature FC- and ZFC-susceptibility obtained for a

5 mT field applied along two crystallographical directions. A sharp increase of the low temperature susceptibility upon cooling is followed by a cusp-like transition at 16 K. This observation, along with a pronounced difference between FC- and ZFC-curves for each field direction suggests the cusp to denote a spin-glass-like transition. The data also reveal an Ising-like anisotropy with easy-axis along the c -axis, and a second anomaly discerned around 11 K perhaps indicating a spin reorientation. The saturation magnetization M_s for fields along c is reached by ~ 0.5 T at $2.45 \mu_B/\text{Pr}^{3+}$. For fields in the ab plane, the magnetization increases slowly, reaching a value of just $0.82 \mu_B/\text{Pr}^{3+}$ by 5 T. For both field directions, a hysteresis is observed with a coercivity of $h_c \sim 60$ mT/ ~ 0.1 T and a remanence of $\sim 1.135 \mu_B$ for fields along c and $\sim 0.04 \mu_B$ for fields in the ab plane.

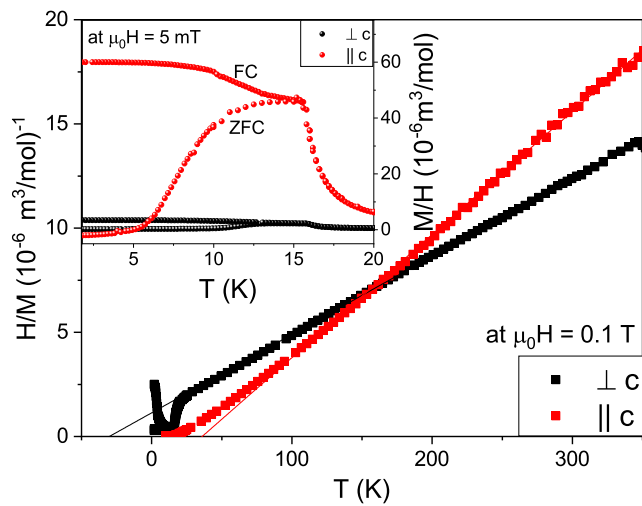


Figure 11. Bulk magnetic property data obtained on a PrAlGe single crystal. The susceptibility was recorded in the range of 1.8 - 400 K with the field aligned perpendicular (black dots) and parallel to c (red dots). The main panel shows the inverse susceptibility measured after FC at 0.1 T. The inset depicts the low temperature range of both ZFC and FC curves measured at 5 mT.

Besides the indication for a spin-glass state below 16 K given by a large splitting of FC- and ZFC-magnetization, we observed a frequency-dependent ac susceptibility of the cusp anomaly at 16 K. The data in figure 12 show the cusp anomaly moves to higher temperatures as the ac frequency is increased, consistent with typical behavior for a spin- or cluster-glass [23]. Taken together, the magnetic measurements suggest PrAlGe to enter a spin-glass state below 16 K, the origin of which may be due to frustration induced by competing ferromagnetic and antiferromagnetic interactions.

Similarly as for CeAlGe, PrAlGe single crystals obtained via the flux method proved to be Al-rich. However, the influence of stoichiometric variance is not as strong as with the Ce ions since there is no structure-

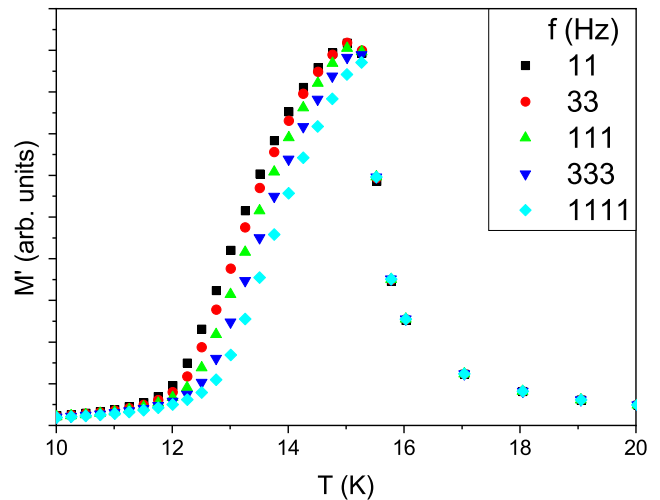


Figure 12. Temperature dependent AC magnetisation measured on a PrAlGe single crystal at a frequency of 11, 33, 111, 333, 1111 Hz with respect to the crystal oriented along the a -direction.

type transition in the $\text{PrAl}_x\text{Ge}_{2-x}$ ($0.8 < x < 1.4$) series [18]. The general magnetic properties of both flux and floating zone grown PrAlGe crystals are similar, but a slight shift of the transition temperature is apparent (see the inset of figure 13).

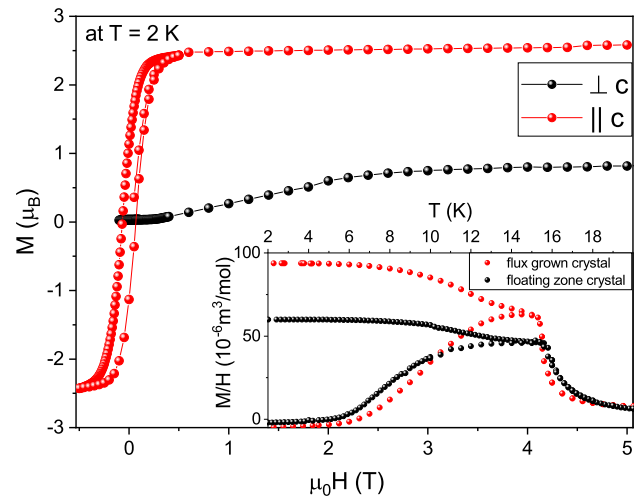


Figure 13. Field dependent magnetisation measured on a PrAlGe single crystal at 2 K after ZFC, for both field directions: perpendicular (black) and parallel to c (red). The inset shows a comparison of the low temperatures susceptibility of a flux grown crystal (5.4 mg) with a floating zone grown crystal (101 mg) measured at 5 mT with the field applied along the c axis.

Temperature dependent resistivity data obtained for a floating zone grown PrAlGe crystal of mass 77.3 mg is shown in Fig. 14. The resulting residual resistivity ratio (RRR) is estimated to be 1.73, and thus similar

to CeAlGe. The spin-glass-like transition is visible in the resistivity as a slight kink just below ~ 16 K. The inset of figure 14 shows the field dependent resistivity for fields applied along the c -axis to be featureless over the explored range measured at 2 K.

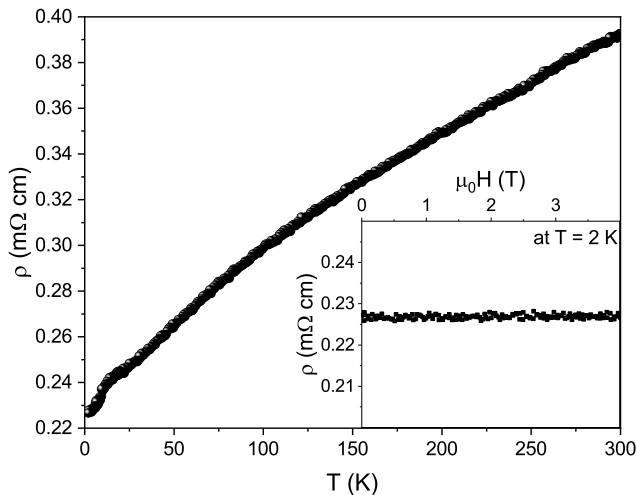


Figure 14. Temperature dependent resistivity with a current along the a -axis of an oriented piece cut from a 77.3 mg floating zone grown PrAlGe single crystal. The inset shows the field dependent resistivity with a field aligned along the c -axis ($H||c$).

VII. SUMMARY

To summarize, we have presented a methodology to grow large crystals of the magnetic Weyl semimetal candidates $RAlGe$ ($R=Ce,Pr$) using the floating zone technique. Due to the inherent flexibility of RAl_xGe_{2-x} , it proves challenging to obtain a perfect 1:1:1 stoichiometry, and slight variations influence both the structural as well as the physical properties. Nevertheless, we reveal both CeAlGe and PrAlGe to crystallize in the SI-breaking polar tetragonal $I4_1md$ structure, thus satisfying the expectation that these systems host Weyl fermions in their magnetically-ordered ground states. The typical RRR values in between 1 - 2 and a resistivity of ~ 0.1 m Ω cm suggest the two materials to be semimetals.

From bulk magnetic characterization, we find PrAlGe to be spin-glass-like below 16 K with a spin reorientation around 11 K and an easy-axis along c . CeAlGe displays a rich magnetic phase diagram characterized by an anti-ferromagnetic ground state below 5 K, with the moments lying in the ab -plane. We find neither of the systems to display the simple ferromagnetic ground state expected according to theory [15]. This renders the anticipated topological phase more complicated, but may nonetheless open the door to new phenomena in topological semimetals linked to complex magnetic ground states. In this

context the prepared crystals provide the foundations for future detailed characterization of the magnetic ground states by transport and microscopic probes aimed at revealing the relation between magnetism and the properties of the Weyl state. The availability of large crystals enables their rich characterisation by microscopic probes such as neutron and photon scattering.

We thank C. Krellner for the provision of measurement time using the SEM. D. Destraz and J. Chang for discussions and support from L. Berardo, I. Zivkovic and H. Rijćenow. The authors would like to acknowledge the Swiss National Science Foundations (SNSF R'Equip, Grant No. 206021_163997 and Grant No. 206021_139082) and matching funds from Paul Scherrer Institute for purchasing SCIDRE HKZ - high pressure high-temperature optical floating zone furnace, the SCIDRE KTS - levitation melting facility and the MPMS as well as funding from the SNSF Sinergia network "NanoSkyrmionics" (grant no. CRSII5-171003).

* pascal.puphal@psi.ch

† jonathan.white@psi.ch

‡ ekaterina.pomjakushina@psi.ch

- [1] H. Weyl, *Zeitschrift für Physik* **56**, 330 (1929).
- [2] S.-Y. Xu, I. Belopolski, N. Alidoust, M. Neupane, G. Bian, C. Zhang, R. Sankar, G. Chang, Z. Yuan, C.-C. Lee, S.-M. Huang, H. Zheng, J. Ma, D. S. Sanchez, B. Wang, A. Bansil, F. Chou, P. P. Shibayev, H. Lin, S. Jia, and M. Z. Hasan, *Science* **349**, 613 (2015).
- [3] B. Lv, H. Weng, B. Fu, X. Wang, H. Miao, J. Ma, P. Richard, X. Huang, L. Zhao, G. Chen, Z. Fang, X. Dai, T. Qian, and H. Ding, *Physical Review X* **5** (2015), 10.1103/physrevx.5.031013.
- [4] S.-Y. Xu, N. Alidoust, I. Belopolski, Z. Yuan, G. Bian, T.-R. Chang, H. Zheng, V. N. Strocov, D. S. Sanchez, G. Chang, C. Zhang, D. Mou, Y. Wu, L. Huang, C.-C. Lee, S.-M. Huang, B. Wang, A. Bansil, H.-T. Jeng, T. Neupert, A. Kaminski, H. Lin, S. Jia, and M. Z. Hasan, *Nature Physics* **11**, 748 (2015).
- [5] M. Z. Hasan, S.-Y. Xu, and G. Bian, *Physica Scripta* **T164**, 014001 (2015).
- [6] M. Z. Hasan, S.-Y. Xu, I. Belopolski, and S.-M. Huang, *Annual Review of Condensed Matter Physics* **8**, 289 (2017).
- [7] C. R. Rajamathi, U. Gupta, N. Kumar, H. Yang, Y. Sun, V. Šabek, C. Shekhar, M. Schmidt, H. Blumtritt, P. Werner, B. Yan, S. Parkin, C. Felser, and C. N. R. Rao, *Advanced Materials* **29**, 1606202 (2017).
- [8] A. Politano, G. Chiarello, Z. Li, V. Fabio, L. Wang, L. Guo, X. Chen, and D. W. Boukhvalov, *Advanced Functional Materials* **28**, 1800511 (2018).
- [9] C.-K. Chan, N. H. Lindner, G. Refael, and P. A. Lee, *Physical Review B* **95** (2017), 10.1103/physrevb.95.041104.
- [10] E. J. Sie, C. M. Nyby, C. D. Pemmaraju, S. J. Park, X. Shen, J. Yang, M. C. Hoffmann, B. K. Ofori-Okai, R. Li, A. H. Reid, S. Weathersby, E. Mannebach, N. Finney, D. Rhodes, D. Chenet, A. Antony, L. Balicas, J. Hone, T. P. Devereaux, T. F. Heinz, X. Wang, and A. M. Lindenberg, *Nature* **565**, 61 (2019).

- [11] T. Suzuki, R. Chisnell, A. Devarakonda, Y.-T. Liu, W. Feng, D. Xiao, J. W. Lynn, and J. G. Checkelsky, *Nature Physics* **12**, 1119 (2016).
- [12] E. Liu, Y. Sun, N. Kumar, L. Muechler, A. Sun, L. Jiao, S.-Y. Yang, D. Liu, A. Liang, Q. Xu, J. Kroder, V. Šafránek, H. Borrmann, C. Shekhar, Z. Wang, C. Xi, W. Wang, W. Schnelle, S. Wirth, Y. Chen, S. T. B. Goennenwein, and C. Felser, *Nature Physics* (2018), 10.1038/s41567-018-0234-5.
- [13] K. Kim, J. Seo, E. Lee, K.-T. Ko, B. S. Kim, B. G. Jang, J. M. Ok, J. Lee, Y. J. Jo, W. Kang, J. H. Shim, C. Kim, H. W. Yeom, B. I. Min, B.-J. Yang, and J. S. Kim, *Nature Materials* **17**, 794 (2018).
- [14] Y. Tokura, M. Kawasaki, and N. Nagaosa, *Nature Physics* **13**, 1056 (2017).
- [15] G. Chang, B. Singh, S.-Y. Xu, G. Bian, S.-M. Huang, C.-H. Hsu, I. Belopolski, N. Alidoust, D. S. Sanchez, H. Zheng, H. Lu, X. Zhang, Y. Bian, T.-R. Chang, H.-T. Jeng, A. Bansil, H. Hsu, S. Jia, T. Neupert, H. Lin, and M. Z. Hasan, *Physical Review B* **97** (2018), 10.1103/physrevb.97.041104.
- [16] S. Dhar, S. Patalwar, and R. Vijayaraghavan, *Journal of Magnetism and Magnetic Materials* **104-107**, 1303 (1992).
- [17] S. Dhar and S. Patalwar, *Journal of Magnetism and Magnetic Materials* **152**, 22 (1996).
- [18] E. Gladyshevskii, N. Nakonechna, K. Cen-zual, R. Gladyshevskii, and J.-L. Jorda, *Journal of Alloys and Compounds* **296**, 265 (2000).
- [19] S. Bobev, P. H. Tobash, V. Fritsch, J. D. Thompson, M. F. Hundley, J. L. Sarrao, and Z. Fisk, *Journal of Solid State Chemistry* **178**, 2091 (2005).
- [20] H. Flandorfer, D. Kaczorowski, J. Gröbner, P. Rogl, R. Wouters, C. Godart, and A. Kostikas, *Journal of Solid State Chemistry* **137**, 191 (1998).
- [21] H. Hodovanets, C. J. Eckberg, P. Y. Zavaliy, H. Kim, W.-C. Lin, M. Zic, D. J. Campbell, J. S. Higgins, and J. Paglione, *Physical Review B* **98** (2018), 10.1103/physrevb.98.245132.
- [22] B. Chen, X. Duan, H. Wang, J. Du, Y. Zhou, C. Xu, Y. Zhang, L. Zhang, M. Wei, Z. Xia, C. Cao, J. Dai, M. Fang, and J. Yang, *npj Quantum Materials* **3** (2018), 10.1038/s41535-018-0114-3.
- [23] J. A. Mydosh, *Reports on Progress in Physics* **78**, 052501 (2015).
- [24] X. Wan, A. M. Turner, A. Vishwanath, and S. Y. Savrasov, *Physical Review B* **83** (2011), 10.1103/physrevb.83.205101.
- [25] L. Lu, Z. Wang, D. Ye, L. Ran, L. Fu, J. D. Joannopoulos, and M. S. i, *Science* **349**, 622 (2015).
- [26] X. Huang, L. Zhao, Y. Long, P. Wang, D. Chen, Z. Yang, H. Liang, M. Xue, Weng, Z. Fang, X. Dai, and G. Chen, *Physical Review X* **5** (2015), 10.1103/physrevx.5.031023.
- [27] W. Hermes, U. C. Rodewald, B. Chevalier, and R. Pötgena, *Zeitschrift für Naturforschung B* **62**, 613 (2007).